5

Multiscale modeling of the structure and properties of ceramic nanocomposites

V. TOMAR, Purdue University, USA

Abstract: One of the most recent developments in ceramics has been the distribution of multiple phases in a ceramic composite at the nanoscopic length scale. An advanced nanocomposite microstructure such as that of polycrystalline silicon carbide (SiC)–silicon nitride (Si_3N_4) nanocomposites contains multiple length scales with grain boundary thickness of the order of 50 nm, SiC particle sizes of the order of 200–300 nm and Si_3N_4 grain sizes of the order of 0.8–1.5 μm. Designing the microstructure of such a composite for a targeted set of material properties is, therefore, a daunting task. Since the microstructure involves multiple length scales, multiscale analyses based material design is an appropriate approach for such a task. With this view, this chapter presents an overview of the current state of the art and work performed in this area.

Key words: ceramic nanocomposites, microstructure, multiple length scales, multiscale modeling.

5.1   Introduction

Over the past half century, ceramics have received significant attention as candidate materials for use as structural materials under conditions of high loading rates, high temperature, wear, and chemical attack that are too severe for metals. However, the inherent brittleness of ceramics has prevented their wide use in different applications. Significant scientific effort has been directed towards making ceramics more flaw-tolerant through design of their microstructures by:

153

- incorporation of fibers or whiskers that bridge the crack faces just behind the crack tip
- designing microstructures with elongated grains that act as bridges between crack faces just behind the crack tip
- incorporating second phase particles, which deflect the crack, making it travel a more tortuous path
- incorporating secondary phases that undergo stress-induced volume expansion that forces the crack faces together.

However, one of the most recent developments has been the distribution of multiple phases in a ceramic composite at the nanoscopic length scale. Owing to the prevalence of nanoscopic features, such composites are referred to as ceramic nanocomposites.

The definition of nanocomposite material has broadened significantly to encompass a large variety of systems such as one-dimensional (1D), two-dimensional (2D), three-dimensional (3D) and amorphous materials, made of distinctly dissimilar components and mixed at the nanometer scale. The general class of nanocomposite organic/inorganic materials is a fast-growing area of research. Reducing the sizes of structural features in materials leads to a significant increase in the portion of surface/interface atoms. The surface/interface energy essentially controls the properties of a solid of such type. Interfaces provide a means to introduce non-homogeneity in the material. This non-homogeneity acts as a significant modification of both thermal and mechanical properties of the composites. Selective mixing of materials in a highly tailored morphology with a high percentage of interface area leads to materials with enhanced properties. The properties of nanocomposite materials depend not only on the properties of their individual parents but also on their morphology and interfacial character-istics.

Nanocomposites find their use in various applications because of the improvements in the properties over the simpler structures. As an example, for components used in a gas turbine engine, a lifetime up to 10 000 h and a retained strength of ~300 MPa at a temperature of 1400°C have been postulated, together with negligible creep rate. Furthermore, at elevated temperatures, the material must exhibit high resistance to thermal shock, oxidation, and subcritical crack growth. Ceramic nanocomposites have been shown to be extremely important for such future applications. Advanced bulk ceramic composite materials that can withstand high temperatures ($> 1500°C$) without degradation or oxidation can also be used for applications such as structural parts of motor engines, catalytic heat exchangers, nuclear power plants, and combustion systems, besides their use in fossil energy conversion power plants. These hard, high-temperature-
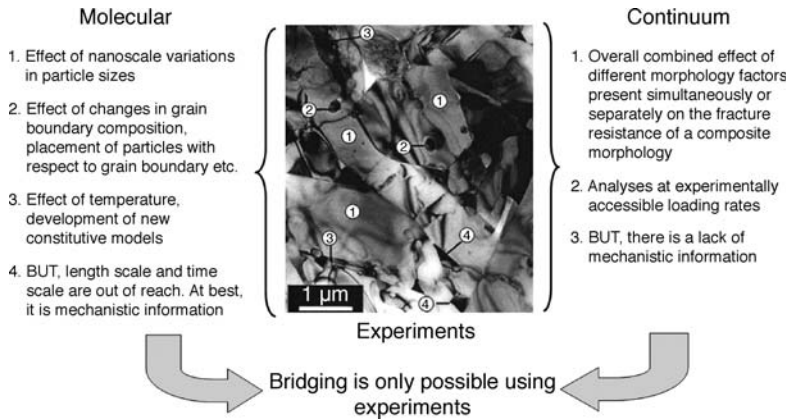
stable, oxidation-resistant ceramic composites and coatings are also in demand for aircraft and spacecraft applications.

One such material system in this class of composites, silicon carbide/silicon nitride (SiC/Si_3N_4) composites, has been shown to perform very well under high-temperature oxidizing conditions. Interest in such nanocomposites started with the experiments of Niihara [1] who reported large improvements in both the fracture toughness and the strength of materials by embedding nanometer range (20–300 nm) particles within a matrix of larger grains and at the grain boundaries (GBs). A 200% improvement in both strength and fracture toughness, better retention of strength at high temperatures, and better creep properties were observed. An advanced nanocomposite microstructure such as that of polycrystalline silicon carbide (SiC)–silicon nitride (Si_3N_4) nanocomposite contains multiple length scales with GB thickness of the order of 50 nm, SiC particle sizes of the order of 200–300 nm and Si_3N_4 grain sizes of the order of 0.8 to 1.5 μm [2]. Designing the microstructure of such a composite (and similar others such as TiN–Si_3N_4, SiC–Al_2O_3, SiC–SiC, graphene/CNT + SiC, and carbon fiber + SiC nanocomposites) for a targeted set of material properties is, therefore, a daunting task. Since the microstructure involves multiple length scales, multiscale analyses based material design is an appropriate approach for such a task.
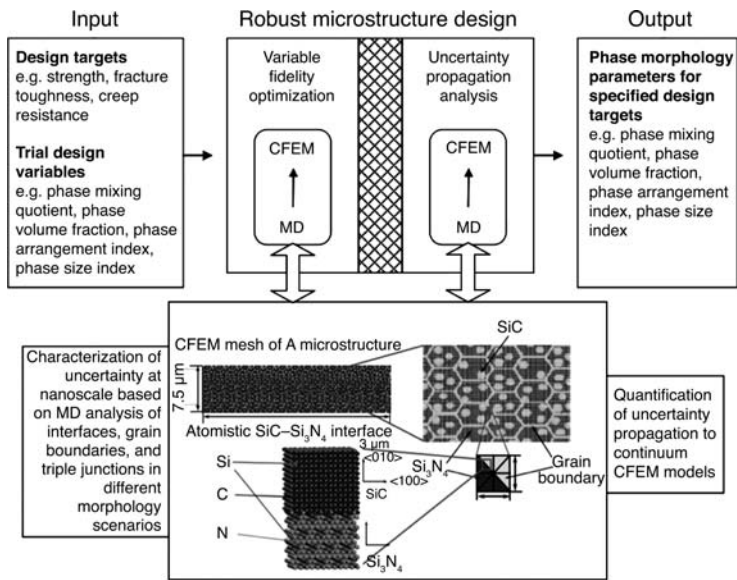
5.2   Multiscale modeling and material design

A multiscale modeling paradigm is shown in Fig. 5.1. Atomistic analyses at the nanoscale can impart important information about the effect of critical features such as a grain boundary (GB), an interface, or a triple junction, etc. on mechanical deformation behavior of a small nanoscale (~ few nanometers) sample. In multiscale modeling such information is used to formulate macroscale (> a few micrometers) material models for understanding microstructure-dependent deformation behavior of a material sample such as the one shown in Fig. 5.1. Appropriate mathematical models of microstructure property relations allow one to relate performances such as fracture toughness, ultimate strength, fatigue lifetime, etc. to key material microstructure parameters like volume fraction, particle size, and phase composition.

Since a typical nanoscale test sample is much smaller and is subjected to varied surroundings in a typical microstructure (e.g. Fig. 5.1), the incorporation of nanoscale information in macroscale models is subjected to statistical uncertainty. If a complex microstructure is to be designed for a targeted set of properties, it is important that such uncertainties be correctly quantified and incorporated within a robust material design framework. The development of a variable fidelity model management framework that can

Molecular

1. Effect of nanoscale variations in particle sizes

2. Effect of changes in grain boundary composition, placement of particles with respect to grain boundary etc.

3. Effect of temperature, development of new constitutive models

4. BUT, length scale and time scale are out of reach. At best, it is mechanistic information

Continuum

1. Overall combined effect of different morphology factors present simultaneously or separately on the fracture resistance of a composite morphology

2. Analyses at experimentally accessible loading rates

3. BUT, there is a lack of mechanistic information

Experiments

Bridging is only possible using experiments

5.1 Multiscale modeling paradigm.

Input

Design targets
e.g. strength, fracture toughness, creep resistance

Trial design variables
e.g. phase mixing quotient, phase volume fraction, phase arrangement index, phase size index

Robust microstructure design

Variable fidelity optimization

CFEM

MD

Uncertainty propagation analysis

CFEM

MD

Output

Phase morphology parameters for specified design targets
e.g. phase mixing quotient, phase volume fraction, phase arrangement index, phase size index

Characterization of uncertainty at nanoscale based on MD analysis of interfaces, grain boundaries, and triple junctions in different morphology scenarios

CFEM mesh of A microstructure
7.5 μm
SiC
Atomistic SiC–Si$_3$N$_4$ interface
3 μm
Si
C
N
<010>
<100>
Si$_3$N$_4$
SiC
Grain boundary
Si$_3$N$_4$

Quantification of uncertainty propagation to continuum CFEM models

5.2 Schematic petascale material design framework.

incorporate material behavior analyses at multiple length scales in a design optimization framework has been reported [3–6].

Figure 5.2 details the process flow of a petascale multiphysics model management tool for multiscale material design. Deployed on a petascale machine, the design tool developed in this research, that integrates atomistic and mesoscale analyses using a variable fidelity model management framework, will facilitate a significant reduction in nanomaterials' development cost and time with a simultaneous increase in the possible different
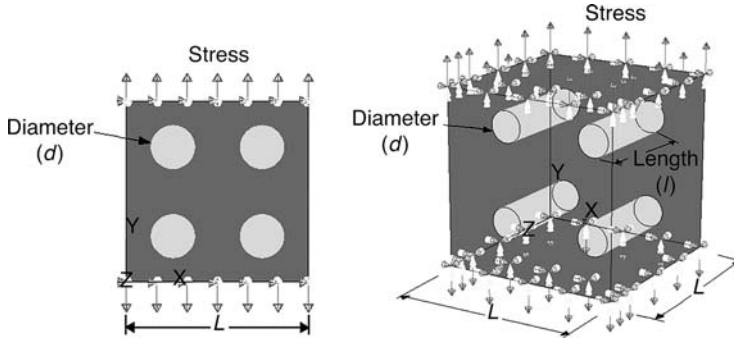
5.3 High- and low-fidelity models for CFCC nanocomposites.

combinations of individual composite material phases to achieve desired material performance. The model management framework [3, 4], besides managing the models and scales, is also well suited to control hierarchical parallelism. The natural hierarchy is molecular dynamics (MD) within the cohesive finite element method (CFEM) within design under uncertainty, using a mixed programming model SHMEM^{TM} by SGI for CFEM and MPI for MD and the uncertainty modeling. Both MD and the uncertainty quantification (via quasi-Monte Carlo integration) can use 1000 processors, and CFEM 10, so 1000 uncertainty quantification groups of 10 CFEM groups of 1000 HMC processors is 10^7 processors, nearing exascale.

Material design analyses of the model system have been performed to understand the morphology-related parameters that must be controlled for optimal targeted set of properties. The application of the design tool is focusing on the continuous fiber ceramic composite (CFCCs) models of SiC–Si$_3$N$_4$ nanocomposites (Fig. 5.3). The second phase (circles and cylinders) are the SiC fibers that have higher elastic modulus and higher creep resistance (E) but lower yield stress and fracture toughness, than that of the primary Si$_3$N$_4$ phase. The problem is to design the most suitable CFCC, with maximum strength and creep resistance for a set of external temperatures T, where the number of design variables will depend on whether the simulation tests are run on the 2D or 3D model. The design variables to be considered in the nanocomposite design optimization problem, for the 2D model, are the fiber diameter (d) and the external temperature (T). For the 3D model, the design variables to be considered are the fiber diameter (d), the length of fibers (l) and the external temperature (T). The problem definition in standard form is:

$$\left. \begin{aligned} &\text{minimize: } f(d,\, l,\, T) = \{-\sigma_{\mathrm{U}}(d,\, l,\, T),\ \varepsilon_{\mathrm{c}}(d,\, l,\, T)\} \\ &\text{subject to: } d_{\min} \leq d \leq d_{\max} \quad l_{\min} \leq l \leq l_{\max} \text{ and } T = 1500^{\circ}\text{C} \end{aligned} \right\} [5.1]$$
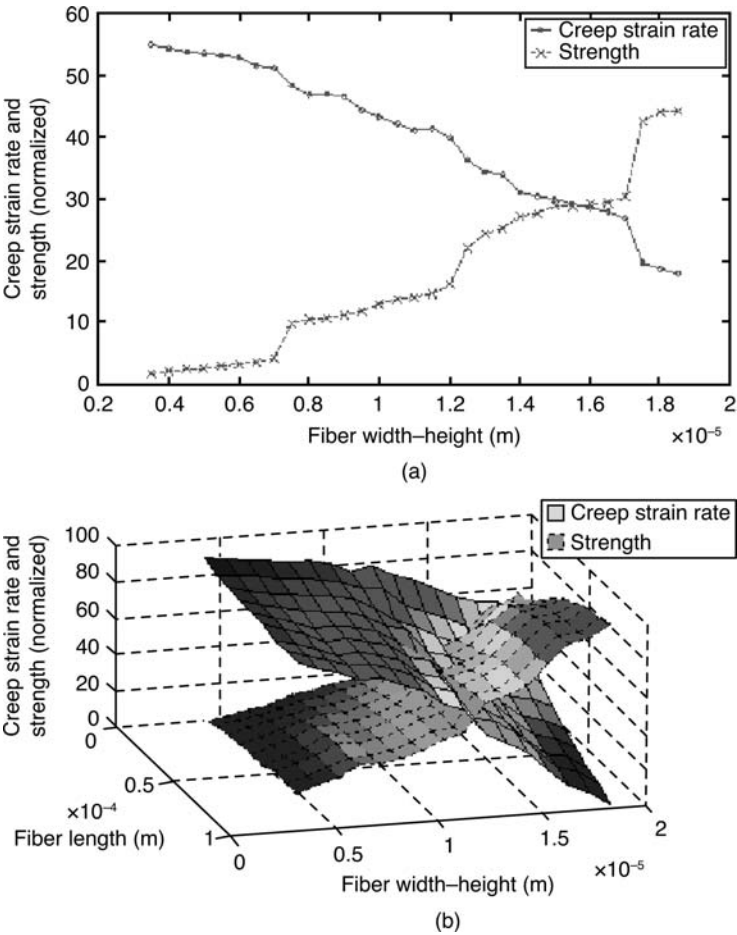
5.4 (a) Strength and creep strain rate at 1500°C as a function of the design variable width–height (*d*) for the 2D low-fidelity model. (b) Strength and creep strain rate at 1500°C as a function of the design variables width–height (*d*) and length of fibres (*l*) for the 3D high-fidelity model.

Figure 5.4 illustrates normalized (0–100) function values for the strength and creep strain rate as a function of design variables for the high-fidelity model (3D) and low-fidelity model (2D). Figure 5.4(a) shows an increase in the CFCC strength and a corresponding decrease in the creep strain rate as the design variable *d* increases. Similarly, for the high-fidelity model, Fig. 5.4(b) shows an increase in the CFCC strength and a corresponding decrease in the creep strain rate as the design variables *d* and *l* increase.
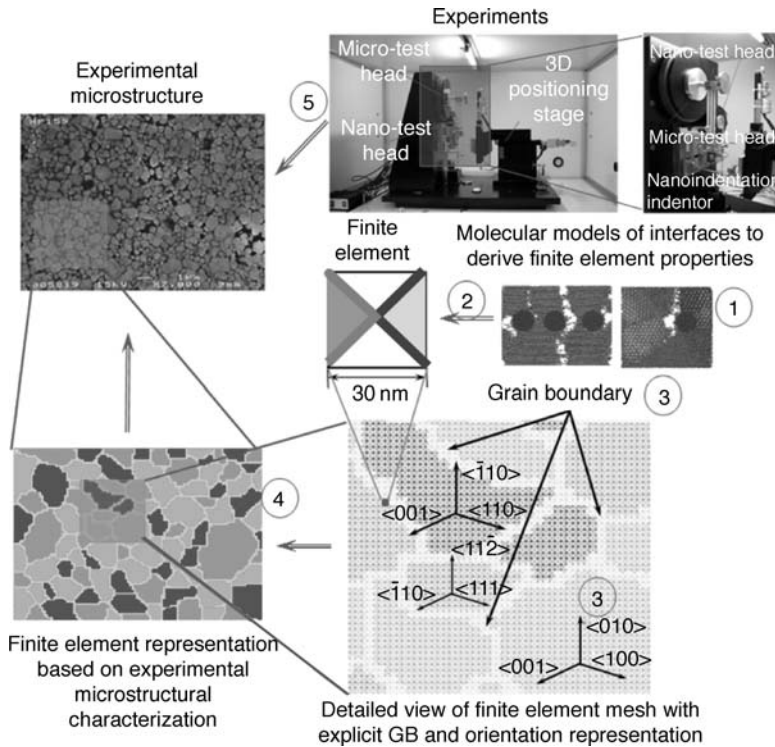
5.5 Multiscale modeling approach.

5.3   Multiscale modeling approach

The multiscale analyses (at nanometer and micrometer length and time scales) are based on a combination of CFEM and MD based techniques as shown in Fig. 5.5. In such analyses we extract information between multiple phases of a material based on molecular simulations. Such information is usually not available in experiments, but is incorporated in continuum models and later compared and validated with experiments.

Several studies have shown that the incorporation of SiC nanoparticles in a Si_3N_4 matrix improves high-temperature creep resistance while maintaining or improving the room-temperature strength [e.g. 1, 2, 7–14]. Following this observation, innovative processing approaches using polymer-derived amorphous Si–C–N powders have been developed to produce *in-situ* SiC nanoparticle reinforced composites [11, 14–19]. While the material system is an excellent candidate for high-temperature applications, a careful analysis of the effect of the underlying morphology on the overall high-temperature behavior of the material system is lacking. Such studies exist for composites in which the reinforcement size is in the several-micron range and, in these

studies, both the reinforcement size and volume fraction significantly affect the fracture toughness and strength [20]. A fundamental understanding of the effect of nanosized SiC reinforcements on the mechanical behavior of Si_3N_4 matrix composites is required before further attempting to improve the properties of these composites by varied morphological alterations in experiments.

Tomar [21, 22] reported on the effect of morphological variations in second-phase SiC particle placement and GB strength on the dynamic fracture strength of SiC–Si_3N_4 nanocomposites using continuum analyses based on a mesoscale cohesive finite element method (CFEM). It was found that high-strength and relatively small sized SiC particles act as stress concentration sites in the Si_3N_4 matrix, leading to intergranular Si_3N_4 matrix cracking as a dominant failure mode. However, as a result of a significant number of nanosized SiC particles being present in microsized Si_3N_4 matrix, the SiC particles invariantly fall in wake regions of microcracks, leading to significant structural strength. This mechanism was further examined using 3D molecular dynamics (MD) simulations of crack propagation in SiC–Si_3N_4 nanocomposites with cylindrical SiC inclusions.

In the case of SiC–Si_3N_4 nanocomposites, MD analyses have also revealed that the second-phase particles act as significant stress raisers in the case of single crystalline Si_3N_4 phase matrix, affecting the strength significantly. However, the particles' presence does not have a significant effect on the mechanical strength of bicrystalline or nanocrystalline Si3N4 phase matrices. The strength of the SiC–Si_3N_4 nanocomposite structures showed an uncharacteristic correlation between GB thickness and temperature. The strength showed a decrease with increase in temperature for structures having thick GBs having diffusion of C, N, or Si atoms. However, for structures with no appreciable GB thickness (no diffusion of C, N, or Si atoms), due to particle clustering and increase in SiC–Si_3N_4 interfacial strength with temperature, the strength improved with an increase in temperature. Figure 5.6 shows snapshots of fracture propagation analyses in such nanocomposites obtained using the CFEM. Current research work focuses on obtaining experimental images of the ceramic nanocomposites developed by collaborators, developing nanoscale CFEM meshes on such images, and performing failure analyses using the combination of MD and CFEM techniques.

As noted earlier, high-strength and relatively small sized SiC particles act as stress concentration sites in the matrix, leading to intergranular Si_3N_4 matrix cracking as a dominant failure mode. CFEM analyses also revealed that the SiC nanosized particles invariantly fall in wake regions of microcracks, leading to significant mechanical strength. This finding was confirmed in the MD analyses that revealed that particle clustering along the
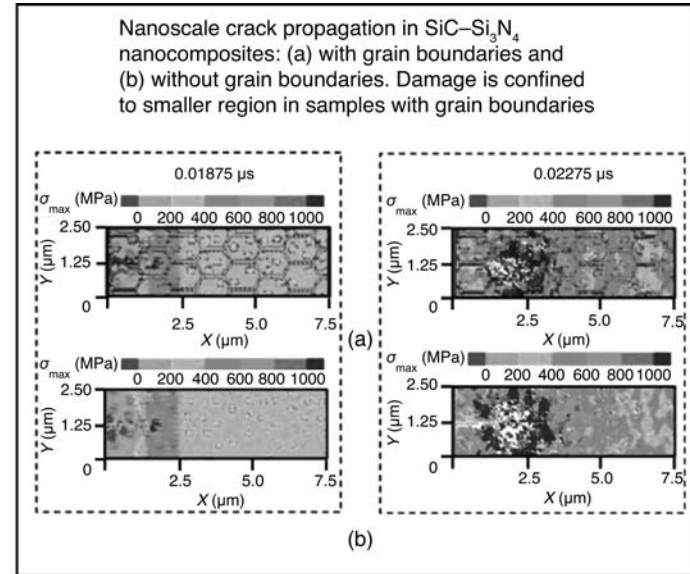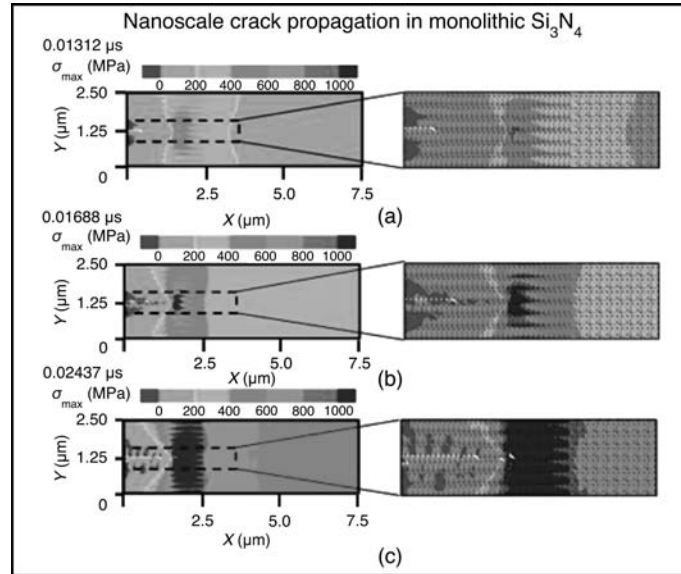
5.6 (a–c) Snapshots of mesoscale crack propagation and damage propagation in SiC–Si$_3$N$_4$ nanocomposites.

GBs significantly increases the strength of these nanocomposites. While some nanocomposite morphologies have sharply defined SiC–Si_3N_4 interfaces [e.g. 23], other nanocomposite morphologies have diffusion of C, N, or Si atoms at the interfaces [e.g. 24].

Classical MD replaces a comprehensive quantum mechanical treatment of interatomic forces with a phenomenological description in the form of an interatomic potential. MD has been used recently to achieve nm/cycle fatigue crack extension rate similar to that observed in experiments [e.g. 25]. The MD simulation results of deformation twinning in two-dimensional nanocrystalline Al with grain sizes from 30 nm to 90 nm by Yamakov and co-workers [26] have been found to be in close agreement with experimental observations reported by Liao *et al.* [27]. MD simulations have proven to provide phenomenological trends on deformation mechanisms of nanocrystalline materials in agreement with experiments [e.g. 28, 29]. Atomistic analyses of the nanocomposite mechanical strength as a function of phase morphology are relatively new and have focused on a very limited set of issues [e.g. 30–34]. Both SiC and Si_3N_4 have been individually analyzed in atomistic simulations for different mechanical strength related issues [e.g. 35–38]. However, SiC–Si_3N_4 nanocomposite morphologies are analyzed in this work for the first time.

5.4   The cohesive finite element method (CFEM)

Molecular dynamics (MD) simulations are performed using a well-established nanocomposite molecular dynamics simulation framework [32, 39]. The CFEM analyses are performed using the analyses criterion developed and reported in [40]. The CFEM is based on continuum mechanical foundations. In the CFEM meshes, each phase is modeled with hyperelastic constitutive behavior based on available experimental evidence [41–44]. In the absence of experimental information, the distribution of the crystalline orientation of the Si_3N_4 and SiC phases is neglected. In the MD morphologies, crystalline orientations are explicitly considered.

The complete CFEM framework has been described earlier [21, 22], so it is only briefly described here. A Lagrangian finite deformation formulation is used to account for the finite strains and rotations in crack tip regions. The CFEM simulations are carried out under plane strain assumption. Although the discussion in the presented research focuses on tensile loading, compression and contact can also be dealt with within this framework [48]. An irreversible bilinear cohesive law is used [21, 22]. Fracture energy per unit cohesive surface area is the same as the fracture energy of the material, Φ_0 (Table 5.1). The damage in cohesive surfaces is tracked through a parameter Φ_d, which is a function of the extent of the separation of cohesive surfaces. $\Phi_d = \Phi_0$ when surfaces have separated to cause fracture. Φ_d is

Table 5.1 Bilinear cohesive law parameters for different phases in microstructures (phase volume fractions $(V_f)_{SiC} = 0.2$ $(V_f)_{Si3N4} = 0.7$ $(V_f)_{GB} = 0.1$)

Component	Φ_0 (N/m)	T^{max} (GPa)	Δ (Nm)	E (GPa)	N	P (kg/m^3)
SiC (SC)	19.53	1.02	38.3	449	0.16	3215
Si$_3$N$_4$ (SN)	191.5	2.3	166.5	210	0.22	2770
Grain boundary (G)	238.7	2.38	200.6	200	0.16	4000
SC-G	19.53	1.02	38.3	—	—	—
SC-SN	19.53	1.02	38.3	—	—	—
SN-G	191.5	2.3	166.5	—	—	—
Homogenized (H)	127.8	2.03	125.9	256.8	0.202	2982
H-SC	19.53	1.02	38.3	—	—	—
H-SN	127.8	2.03	125.9	—	—	—
H-GB	127.8	2.03	125.9	—	—	—

partly converted into the surface energy and partly spent on causing damage in the material adjacent to crack surfaces through microcrack formation that is not based on a pre-specified criterion. A unique damage parameter can be defined to phenomenologicaly track the progressive softening of cohesive surfaces interspersed throughout the composite microstructure. This parameter D is defined such that:

$$D = \frac{\Phi_d}{\Phi_0} \qquad [5.2]$$

Note that $0 \leq D \leq 1$, with $D = 0$ indicating fully recoverable interfacial separation and $D = 1$ signifying complete separation or total fracture. In the numerical analysis carried out by Tomar and co-workers [46, 47], and in the presented research, D is used as a state variable quantifying the degree of the damage, providing a phenomenological measure for failure analysis.

5.4.1 Experiment-based calculation of the bilinear cohesive law parameters

Overall, five parameters are needed to specify the cohesive behavior, including the maximum tensile strength T_{max}, the critical separations Δ_{nc} and Δ_{lc}, characteristic separation η_0 and α. Note that only four of these parameters are independent since $\alpha = \Delta_{nc}/\Delta_{lc}$. Calibration of these parameters is an important aspect in the implementation of the CFEM model. T_{max} is commonly assumed to be a fraction of the Young's modulus (1/100 to 1/1000) [48]. The critical separations Δ_{nc} and Δ_{lc} are usually obtained by equating the area under the cohesive relation to the formation energy per unit area of the corresponding fracture surface. In this regard, experimental efforts have been reported [49, 50]. The value of α is typically

obtained from the ratio between the tangential and normal energy release rates [54].

In this study, the approach for parameter selection as described by Xu and Needleman [48] is used. The value of characteristic separation η_0 is taken as 0.001 [50]. GBs in the nanocomposites have a glassy structure consisting of densification aids such as Y_2O_3 and other rare earth oxides such as samarium, gadolinium, dysprosium, erbium, and ytterbium (verified using the TEM observations on the Si_3N_4 phase [52]). Experimental data on the fracture properties and strength of GBs are not available. The GBs' chemical composition is a complex and uncharacterized combination of different compounds such as Y_2O_3, MgO, etc. with glassy structure. Accordingly, the fracture properties for GBs cannot be specified based on chemical composition. However, experiments for polycrystalline Si_3N_4 have shown that the presence of GBs results in lowering of mechanical strength owing to GB sliding (attributed to glassy structure) and an increase in fracture strength owing to the crack-deflection effect (roughly of the order of 5%) [53]. Accordingly, the GBs are arbitrarily assigned 5% higher fracture strength than that of the Si_3N_4 matrix. An increase in fracture strength for structural and glassy materials is often accompanied with a reduction in elastic modulus. Accordingly, while arbitrary assigning 5% higher fracture toughness to GBs than Si_3N_4 phase, the elastic modulus is made smaller than that of the Si_3N_4 phase by 5%. The immediate effect is that the simulations are qualitative in nature. With the availability of experimental measurements on GB properties, more realistic properties of GBs can be incorporated to increase the accuracy of the simulation predictions.

Because the GBs have finite widths, there are three phases (GBs, SiC, and Si3N4) in the microstructures analyzed. The cohesive parameters are calculated using experimental information on the elastic moduli and Φ_0 [1, 41–44, 54–57]. Homogenized properties are calculated using volume weighted averaging. The values for Φ_0 are obtained based on surface energy release rate measurements during fracture experiments on bulk SiC and Si_3N_4 reported in the literature. An interface between any two of the three phases is assigned the cohesive properties corresponding to the weaker phase. Table 5.1 shows the material properties for analyzing microstructures shown in Fig. 5.6.

5.4.2 CFEM problem setup

Microstructures analyzed using CFEM are shown in Fig. 5.6. Since a given unique set of phase morphology defining parameters (such as the location of SiC particles in the current research) corresponds to multiple sets of phase morphologies, three different random samples corresponding to each

microstructural representation shown in Fig. 5.6 are used to characterize the material behavior. The microstructures have Si_3N_4 grain size approximately equal to 1.2 μm and SiC particle size approximately equal to 200 nm. The volume fraction of the SiC phase is fixed at 20%. The average GB width is approximately 120 nm. Accordingly, the microstructures with GBs have the approximate GB volume fraction of 10%.

To track complex crack/microcrack patterns, arbitrary crack paths and crack branching, cohesive surfaces are specified along all finite element boundaries as an intrinsic part of the finite element model. All cohesive surfaces serve as potential crack paths in the microstructure; therefore, fracture inside each microstructural phase and along interphase boundaries can be explicitly resolved (for more details see [40], [46] and [47]). Accordingly, the analyses are able to take into account the intergranular as well as intragranular fracture.

The finite element meshes used have a uniform structure with 'cross-triangle' elements of equal dimensions arranged in a quadrilateral pattern (Fig. 5.7). This type of triangulation is used since it gives the maximum flexibility for resolving crack extensions and arbitrary fracture patterns [40]. Because of the computational limitations and the requirement that stress wave reflections do not interfere with the analyses results [40], the microstructures are embedded in a uniform finite element mesh (see the mesh surrounding the microstructure in Fig. 5.7). The uniform mesh has elements with higher size increasing the overall size of the sample to delay the stress wave reflection and minimize its effect on dynamic fracture while simultaneously reducing the computational load. Since the crack propagation is limited to the microstructural window whose size had been analyzed in a previous research [40], the results are unaffected by the presence of the uniform mesh.

The dimensions for the microstructural region (7.5 μm × 30 μm) are limited by the memory sizes of the supercomputers used (a 48 processor Opteron Linux cluster in this work). These regions are much larger than the length scales involved in all microstructures. Thus, reasonable representations of the microstructures are achieved. Material outside the microstructure window is assumed to be homogeneous and assigned effective properties representative of those for the SiC–Si_3N_4 ceramic composite. Computations are carried out for side-cracked samples under tensile loading. The length of the initial crack is $a_i = 9.0$ μm. Tensile loading is applied by imposing velocity boundary conditions along the upper and the lower edges of the specimen in the direction shown in Fig. 5.7. The boundary velocity V_0 (0.5 m/sec and 2 m/sec) is imposed on the bottom and top edges with a linear ramp from zero to V_0 in the initial phase of loading. This represents the loading of the pre-crack by a tensile wave with a stress amplitude of $\sigma = \rho \, C_L \, V_0$ (ρ is homogeneous material density and C_L is the
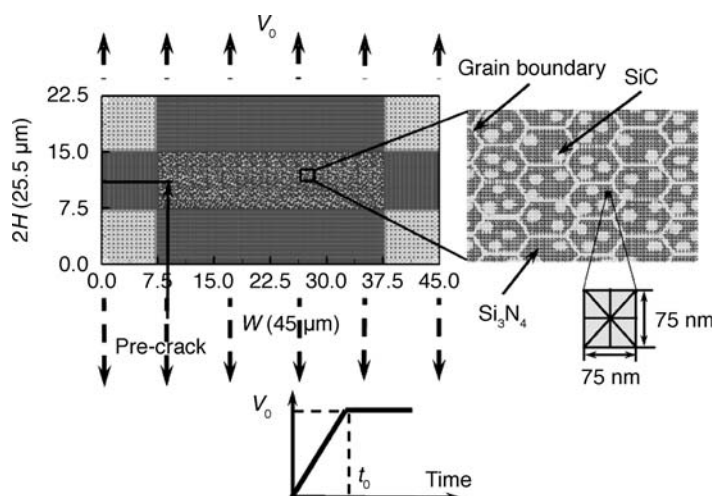
5.7   Dynamic fracture simulation setup with FEM discretization for performing the CFEM simulations.

homogeneous material longitudinal wave velocity) (14.3 MPa and 57.3 MPa at V_0 = 0.5 m/sec and 2 m/sec, respectively) and a linear ramp from zero to that value in the initial phase of loading. The specimen is stress free and at rest initially. Conditions of plain strain are assumed to prevail.

For the CFEM mesh and the bilinear cohesive law used, convergence analyses of the dependence of mesh element size on simulation results have been performed [40]. Based on those analyses, we require the characteristic finite element size, h, to satisfy: 750 nm > $h \geq$ 30 nm. The upper limit is based on the minimum cohesive zone size estimate based on the properties listed in Table 5.1 [40]. The lower limit is based on the elimination of material softening because of the use of bilinear law with finite initial stiffness [40]. The characteristic element size of 75 nm satisfies the convergence criterion. The characteristic size corresponds to four finite elements (Fig. 5.7). Accordingly, there are 542 000 elements in each analyzed finite element mesh.

5.5   Molecular dynamics (MD) modeling

The MD simulations described here were carried out under 3D conditions (using periodic boundary conditions (PBCs)). The focus of the analyses is on understanding the deformation mechanisms in the composites and on delineating the factors affecting their strength. The microstructures analyzed are shown in Fig. 5.8. Six different atomistic morphologies were analyzed: M1 is a 10 nm sized cubic single crystal Si_3N_4 block; M2 a 10 nm sized cubic bi-crystalline Si_3N_4 block; M3 is a microstructure based on M1 with a 3 nm
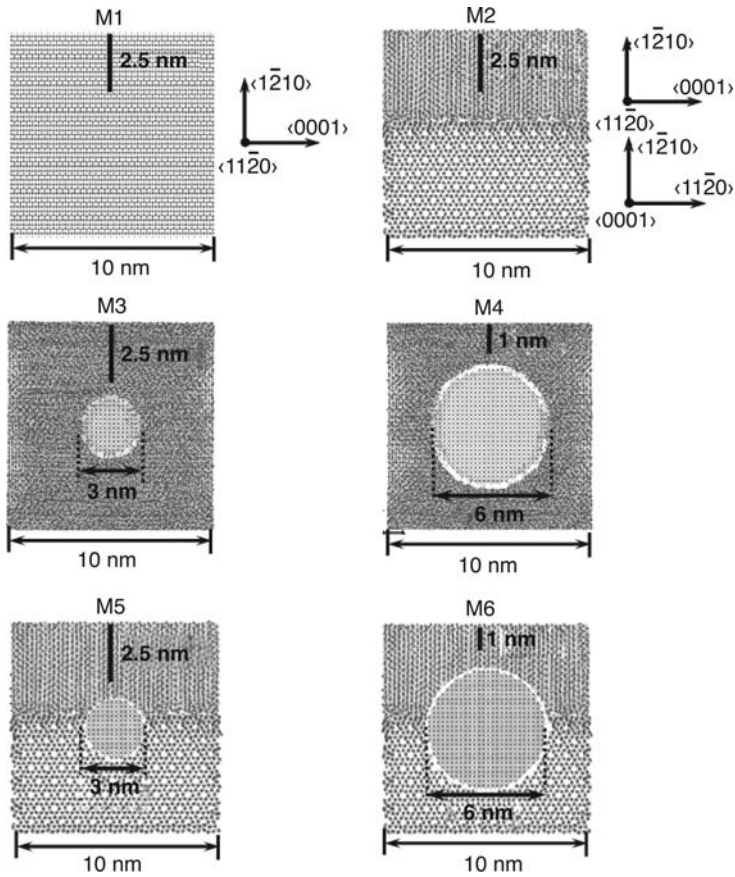
5.8   Atomistic microstructures analyzed for crack propagation.

sized cylindrical inclusion; M4 is based on M1 with 6 nm sized cylindrical inclusion; M5 is based on M2 with 3 nm sized cylindrical inclusion; M6 is based on M2 with 6 nm sized cylindrical inclusion. Because of the imposition of PBCs, microstructures M3 to M6 represent composites with second-phase SiC inclusions arranged periodically. Figure 5.8 also shows crack lengths in the analyzed nanocomposites.

The structures shown in Fig. 5.8 are three-dimensional. The structures were formed by placing SiC cylindrical particles in Si_3N_4 blocks with holes. Setting up of the SiC–Si_3N_4 interface in the structures can critically affect the internal stresses. In order to relieve any artificial internal stresses, first Si_3N_4 blocks with holes were prepared and equilibrated without the presence of the corresponding SiC cylindrical particles. SiC particles that are to be inserted in the Si_3N_4 holes were separately equilibrated as clusters. After equilibration, the Si_3N_4 block and the corresponding SiC particle were put

together to form a SiC–Si_3N_4 composite. Then the composite structure was again equilibrated. A gap of 2 Å was ensured between the SiC particles and the corresponding Si_3N_4 block's hole in order to prevent additional buildup of internal stresses. However, changing the gap did not influence the observed trends and results.

The composites were analyzed for crack propagation as well as for mechanical deformation without an initial crack. The mechanical deformation methodology is based on earlier work by the authors [32, 39]. The initial crack in the nanocomposites was defined by switching of interatomic interactions along the plane shown in Fig. 5.8. After that, mechanical deformation was applied and crack propagation visually followed and analyzed. This methodology for analyzing crack propagation is based on earlier published work [28, 58]. Important elements of the MD framework are now described.

5.5.1   Interatomic potential for SiC–Si_3N_4 material system

Classical MD simulations of $Si_3N_4 + SiC$ material systems require an interatomic potential to describe Si–Si, Si–N, Si–C, N–N, C–C, and N–C interactions. The potential should be fitted to the properties of Si_3N_4, SiC and to an approximation to the interfacial transitions between these components. The silicon nitride family consists of two members, α and β. The higher symmetry β phase has a hexagonal lattice (space groups C_{6h}^2, N176) with a primitive cell containing two Si_3N_4 formula units ($a = 7.606$ Å, $c = 2.909$ Å). The lower symmetry α phase is trigonal (space groups C_{3v}^4, N159) and has a primitive cell nearly twice as large ($a = 7.746$ Å, $c = 5.619$ Å) with twice as many atoms. Both structures consist of a SiN_4 tetrahedron forming a 3D network with each N corner common to three tetrahedra. Each NSi3 polyhedra has a pyramid-like form in the α phase, while the β phase can be regarded as being built of planar N2Si3 and nearly planar N1Si3 triangles with each Si corner common to four triangles that are oriented perpendicular to the direction (001) or along it. The interatomic potentials for the Si_3N_4 material system have been developed elsewhere [37, 59–61]. Fang *et al.* [62] carried out investigations of phonon spectrum and thermal properties in cubic-Si_3N_4.

Of all the above approaches, the potential of Ching *et al.* [61] was chosen to model β-Si_3N_4 because of its simplicity and ability to enable large-scale MD simulations. β-Si_3N_4 was chosen because of its relative abundance in comparison to the α form. Different polytypes of SiC exist at ambient pressure, which are differentiated by the stacking sequence of the tetrahedrally bonded Si–C bilayers [63]. Among these polytypes, β-SiC (cubic-SiC) is of much interest for its electronic properties. In particular, in recent years many theoretical and experimental studies have been carried

out to investigate the different properties and possible applications of this material.

The majority of interatomic potentials developed for SiC material system focus on describing the material properties of β-SiC [e.g. 64–68]. We choose Tersoff's bond order potential to model interatomic interactions in SiC. At the interface of SiC and Si_3N_4, we need to be able to describe Si–C, Si–Si, C–N, and Si–N interactions. Tersoff's potential is useful only for describing the bulk Si–Si, C–C, and Si–C interactions [69]. Accordingly, a pair potential form similar to that used for Si_3N_4 is sought to be used for interfacial interactions at the SiC–Si_3N_4 interfaces. We use the of potentials Marian et al. [70] to describe Si–N, Si–Si interactions, the potential of Vincent and Merz [71] to describe C–N interactions, and the potential of Jian et al. [72] to describe Si–C interactions at the SiC–Si_3N_4 interfaces.

5.5.2 High-performance computing and mechanical deformation algorithm for MD simulations

MD simulations are performed using a modified version of a scalable parallel code, DL_POLY 2.14 [73, 74]. Electrostatic calculations using the code can be carried out for charged as well as neutral systems using well-established algorithms [e.g. 75–77]. The code has been modified and tested on a system of 1 000 000 atoms for a model ceramic matrix composite (Al + Fe_2O_3) material system and is benchmarked for scalable high-performance classical MD simulations for large atomic ensembles with millions of atoms [73, 78].

The simulations primarily focus on obtaining virial stress versus strain relations and visual atomistic deformation information in order to delineate the deformation mechanisms. In previous uniaxial quasistatic deformation analyses of nanocrystalline Cu by Schiøtz et al. [79], strain was calculated by recording the changes in positions of individual atoms. The average virial stress was calculated at every step in order to obtain the stress–strain relations. A modified version of this approach is used here. An alternative method to obtain uniaxial stress–strain curves is to record strain–time curves at several values of applied stress and then deduce the stress–strain relations [80]. Spearot et al. [81] used both methods and found that the modified method [82] works better because it controls the applied strain and closely emulates controlled displacement experiments. The modifications to the method of Schiøtz et al. [79] include the use of a combination of the algorithms for NPT and NVT ensembles. Alternating steps of stretching and equilibration at constant temperature are carried out to approximate uniaxial quasistatic deformation. Initially, the system is equilibrated at a specified temperature (300 K). During equilibration, NVT equations of

motion are used to relax the pressure on structure in all three directions. During stretching, the MD computational cell is stretched in the loading direction using a modified version of the NPT equations of motion [83]. NPT equations ensure that the structure has lateral pressure relaxed to atmospheric values during deformation [32, 39]. In this algorithm, the rate of change of a simulation cell volume, $V(t)$, is specified using a barostat friction coefficient parameter η such that:

$$\frac{d\eta(t)}{dt} = \frac{1}{Nk_B T_{ext}\tau_P^2} V(t)(P - P_{ext}) \tag{5.3}$$

and

$$\frac{dV(t)}{dt} = 3\eta(t)V(t) \tag{5.4}$$

where P is the instantaneous pressure, P_{ext} is the externally applied pressure, N is total number of atoms in the system, k_B is the Boltzmann constant, T_{ext} is the external temperature, and τ_P is a specified time constant for pressure fluctuations. For a given cross-sectional area, the specification of η in equation 5.4 is equivalent to specifying strain rate for the change in simulation cell length. Further, for a given η, equation 5.3 can be modified as:

$$\frac{d\eta(t)}{dt} = \frac{1}{Nk_B T_{ext}\tau_P^2} V(t)(P - P_{ext}) - \gamma\eta \tag{5.5}$$

In equation 5.5, the term $\gamma\eta$ acts as a damping coefficient for reducing fluctuations in pressure during the stretching of the simulation cell. During the simulations, the system is initially equilibrated at $T_{ext} = 300$ K. After equilibration, the computational cell is stretched in the loading direction using $\eta = 0.1$ psec^{-1}. The values of $\gamma = 0.5$ and $P_{ext} = 1$ atmospheric pressure are used.

The values for η and γ are calculated in trial calculations that focused on achieving the best balance between simulation time (low η results in long simulation times and vice versa) and pressure fluctuations (high γ results in excessive pressure damping with increase in residual stresses along periodic boundaries). In the analyses reported in this chapter, the MD equilibration time in between the periods of stretching is chosen as 2.0 psec.

5.6   Dynamic fracture analyses

As pointed out earlier, simulations focus on comparing the CFEM analyses of the effect of the second-phase SiC particles with the MD analyses. MD results are analyzed using visuals as well as virial stress–strain relations.

Virial stress represents internal resistance offered by a material to an externally imposed load [84]. Since virial stress is an internal quantity, it is also an indicator of the increase in the stress concentration caused by the presence of an inhomogenity in an otherwise homogenous body. This characteristic is used to analyze the effect of the cracks in the presented analyses. The focus of the analyses is on developing an understanding of the correlations between particle size, particle placement with respect to a bicrystalline interface and the strength against crack propagation.

Figure 5.9 shows the stress field in a monolithic Si_3N_4 sample of the same size as that of the CFEM meshes shown in Fig. 5.7 as the crack propagates. As shown, the crack tip stress field is resolved using the CFEM mesh used in the research. As shown in the inset, the fine size of the mesh does not allow extreme distortion of the finite elements. In order to understand the stress distribution and damage evolution, the damage parameter (D (equation 5.2)) and the maximum principal stress (σ_{max}) distributions are analyzed in all microstructures. As explained earlier, $0 \leq D \leq 1$, with $D = 0$ indicating fully recoverable interfacial separation and $D = 1$ signifying complete separation or fracture. The results for damage distribution in all three types
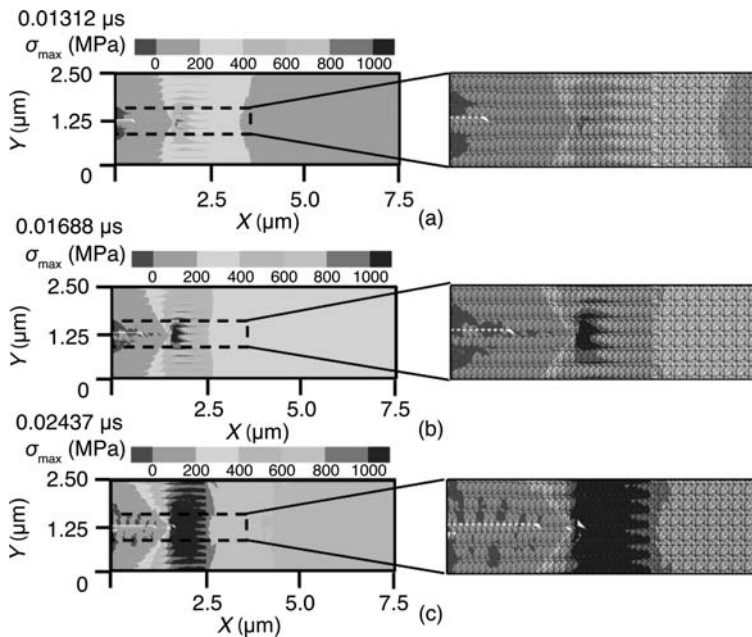

5.9   Stress distribution as a function of damage progression in the case of bulk Si_3N_4 at the loading rate of 2 m/sec at time (a) 0.01312 μsec, (b) 0.01688 μsec, and (c) 0.02437 μsec. The close-up inset in each plot shows how the crack tip stress field is resolved and elements distorted as crack progresses.
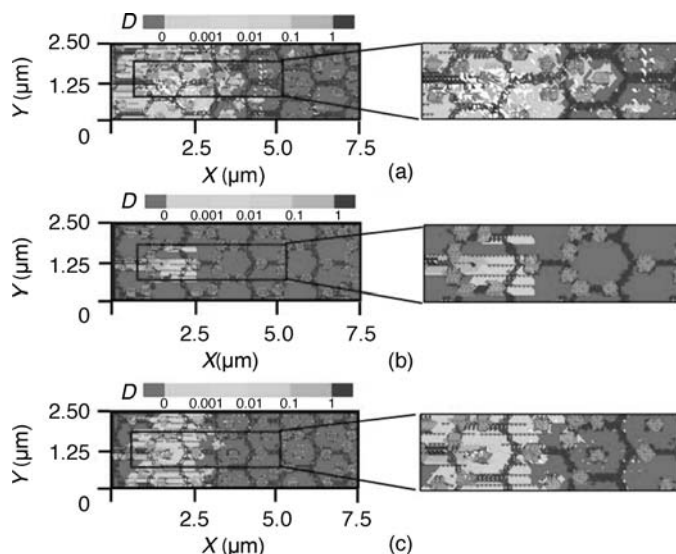
5.10   Damage distribution in (a) Class I, (b) Class II, and (c) Class III microstructures at the loading rate of 2 m/sec and time $t = 0.01875$ μsec. Close-up insets offer higher resolution view of the damage region. Broken particles have distorted 'crumbled' appearance. The intact particles have near circular appearance. Corresponding fragmented GBs show up as zigzag lines in the diffused damage region. These lines are outlines of the fragmented GB elements.

of microstructures at time $t = 0.01875$ μsec (Fig. 5.10) at $V_0 = 2$ m/sec are now discussed.

A concentrated stress field similar to homogeneous materials near the propagating crack tip is seen in all three microstructures. The distribution of stress around the crack tip is strongly affected by the distribution of second-phase SiC particles with respect to Si_3N_4 GBs. The presence of SiC particles inside Si_3N_4 grain interior in the case of Class I and Class III microstructures results in stress concentration over and in excess of the crack tip stresses that are seen in the case of Class II microstructure where the SiC particles are placed solely along GBs. In the case of the Class II microstructure, near crack tip stresses are concentrated in a very small region. This is contrary to the case of the Class I microstructure where the near crack tip stress fields are spread over a larger microstructural region. Owing to the SiC particle stress concentration, intergranular microcracks originating in the microstructure can also be seen. Stress distribution in the Class III microstructure lies in between that of the Class I and Class II microstructures. The effect of the difference in the fracture and bulk properties of GBs and Si_3N_4 matrix on stress distribution is insignificant in comparison to the effect of the second-phase particle placement. GBs are
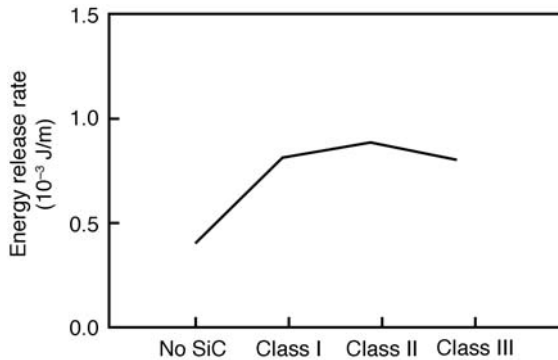
5.11   Mean energy release rate values as a function of microstructure at loading velocity of 2 m/sec. No SiC is a control microstructure with no SiC particles.

shown to restrict the damage to grain interior. However, SiC particles primarily determine how soon the structure develops microcracks.

Self-reinforced Si_3N_4 is an important example of the high-toughness structural ceramics first manufactured during 1970s. Embedding nanosized SiC particles in a Si_3N_4 matrix is one proven approach to improve its mechanical properties. It is also verified here by comparing the average energy release rate of all the microstructures with that of a control microstructure that contains no SiC particles at all (Fig. 5.11). As shown, a significant increase in the fracture resistance is observed. For the first time, Niihara [1] reported almost 200% improvements in both the fracture toughness and the strength of SiC–Si_3N_4 nanocomposites by embedding nanometer size (20–300 nm) particles within a matrix of larger grains and at the Si_3N_4 GBs. Since then, a number of experiments focusing on manufacturing SiC–Si_3N_4 nanocomposites have been reported [2, 53]. So far it has been very difficult to control the processing routes and conditions to place SiC particles selectively along GBs. However, it is possible to place second-phase particles in a combination that places them along GBs as well as in grain interiors near GBs, which may ultimately result in very high strength SiC–Si_3N_4 nanocomposites [14]. Such mechanisms have been observed for other SiC particle reinforced nanocomposites [85, 86].

Figure 5.12 shows stress–displacement plots for atomistic microstructures M1 to M6 in order to compare the internal stresses when an initial crack is present in all microstructures with the internal stresses when the initial crack is absent in all the microstructures. Figures 5.13 and 5.14 show visuals of crack propagation as a function of total displacement for microstructures M1, M2, M4, and M6. The results from Figs 5.12 to 5.14 are now collectively discussed.

As shown in Fig. 5.12(a), microstructures M1 and M2 have the same
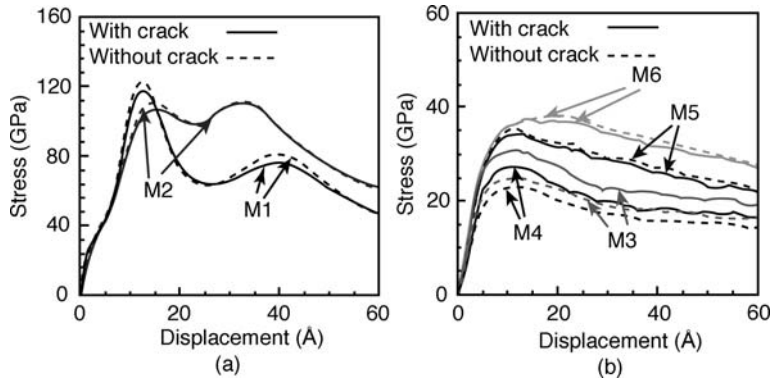
5.12   Virial stress versus displacement plots for (a) microstructures M1 and M2 and (b) microstructures M3, M4, M5, and M6.
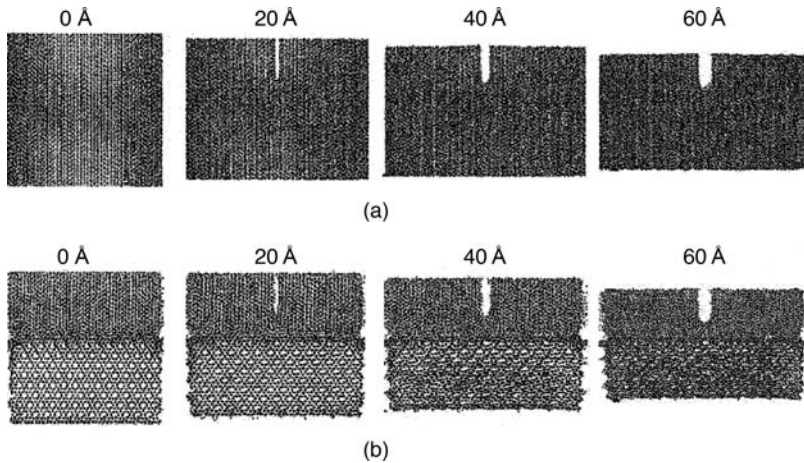
5.13   Crack propagation as a function of displacement for microstructure (a) M1 and (b) M2.

stress–displacement profile with or without initial cracks. Microstructure M2 has an interface, as shown in Fig. 5.8, which leads to lower peak stress values. However, overall, the area under the stress–strain curve in the case of M2 is higher. This indicates that the presence of an interface leads to an increase in toughness for Si_3N_4. The presence of an initial crack does not have any significant effect on the stress–strain profile for both M1 and M2. This may be attributed to the long-range Coulumbic interactions that are not affected by the switching off of interatomic interactions in the crack plane.

As noted earlier, virial stress is an internal quantity signifying the resistance of atomistic system to external load or pressure. In this case,

0 Å   20 Å   40 Å   60 Å

(a)

0 Å   20 Å   40 Å   60 Å

(b)
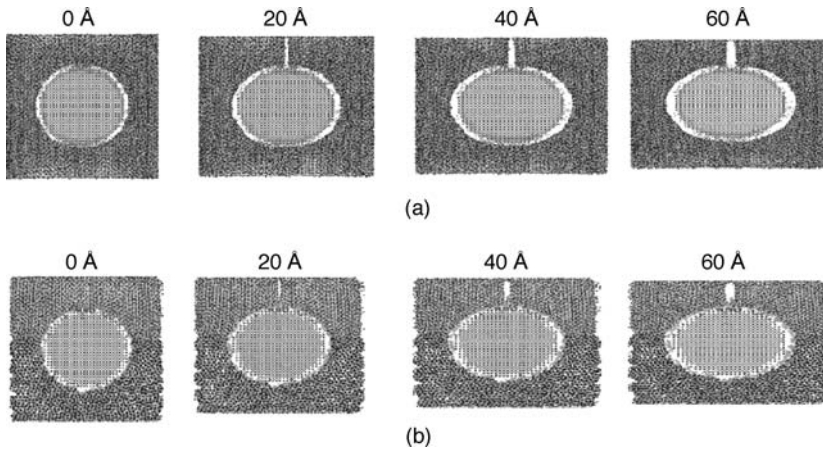
5.14 Crack propagation as a function of displacement for microstructure (a) M4 and (b) M6.

owing to the presence of Coulombic interactions, the presence of nanosized small cracks does not result in appreciable stress concentration. That leads to the stress profiles for a system with and without crack being almost the same. A secondary peak can also be observed in all stress–strain curves in Fig. 5.12(a). This secondary peak may correspond to an internal reorganization in all the microstructures. However, atomistic visualization did not reveal any such changes in the structural features. This is also attributable to the complex hexagonal structure of Si_3N_4, which is extremely difficult to analyze visually. Overall, an important finding from the plots in Fig. 5.12(a) is that the presence of interfaces results in an increase in the overall toughness of the material.

In Fig. 5.12(b), stress–strain plots for M3, M4, M5, and M6 are shown. A direct comparison with the plots in Fig. 5.12(a) reveals that the presence of second-phase SiC particles results in significant weakening of M1 and M2. The effect of the initial crack is also found to be significant. This is apparent by looking at the differences between the curves with initial crack and the ones without initial cracks. It has been pointed out [21] that high strength and relatively small sized SiC particles act as stress concentration sites in Si_3N_4 matrix, leading to intergranular Si_3N_4 matrix cracking as a dominant failure mode. However, as a result of a significant number of nanosized SiC particles being present in the microsized Si_3N_4 matrix, the SiC particles invariantly fall in wake regions of microcracks, which results in significant structural strength. The observations here confirm the first point – that the presence of SiC particles will significantly weaken M1 and M2 against deformation and fracture. A comparison of deformation without initial crack and with initial crack for microstructures M3 and M4 reveals that, in

the absence of an interface in Si_3N_4, the presence of an initial crack will lead to higher internal stresses. The curves also show that internal stresses will decrease with an increase in particle size and the corresponding reduction in the interparticle spacing (owing to the imposed PBCs). The difference between the stresses with and without initial cracks can be explained by a significant stress concentration caused due to the presence of second-phase particles and their interactions with the propagating initial crack. This stress concentration reduces with an increase in particle size, leading to lower internal stresses overall.

In the case of microstructures M5 and M6 with SiC inclusion now placed along a Si_3N_4 interface, a reversal in trend regarding the effects of particle size and initial crack is observed. As was observed earlier in the case of M1 and M2, the presence of a crack does not result in an appreciable stress concentration in M5 and M6. A combined effect of the change in particle size and the presence of an interface is now that the internal stresses rise with an increase in particle size and a reduction in particle spacing. This result is in direct contrast to earlier observations of a reduction in internal stresses with increase in particle size for microstructures M3 and M4. The difference is now the presence of the interface. The interface, while imparting higher toughness for a given particle size, is also a site for structural discontinuity. The presence of second-phase particles with a reduction in spacing between the particles will lead to a stronger material when particles are present along the interface. The trend is reversed when particles are present in the grain interior.

Overall, the combination of observations from Figs 5.12, 5.13, and 5.14 reveals that the effect of interfaces is to strengthen the material by raising toughness. The presence of second-phase particles will lead to a reduction in strength. The presence of nanosized cracks in an ionic material does not offer significant stress concentration until aided by the presence of second-phase inclusions. The toughening of the nanocomposite in the presence of a combination of interfaces and second-phase particles is strongly dependent upon whether the second-phase particles are placed along interfaces or in grain interiors. In addition, the strengthening is also dependent upon the size and relative spacing between particles, irrespective of whether the particles are in grain interiors or at the interfaces. The trend, however, is different for interfaces and grain interiors.

5.7   Conclusions

This chapter has CFEM and MD based analyses to understand the effect of second-phase SiC particles on the strength of SiC–Si_3N_4 nanocomposites. CFEM analyses can explicitly account for the effect of nanoscale inclusions on the strength of nanocomposites. However, the CFEM cannot account for

the effect of nanoscale size changes and nanoscale position changes on the strength of nanocomposites. MD analyses can be very useful to reveal this information, along with information on the effect of interfaces and the mechanism of deformation for certain specific orientations. Overall, CFEM analyses demonstrated that, irrespective of the location of second-phase particles, the final failure mode in all microstructures is brittle fragmentation with initial microcracks forming and propagating mainly in the Si_3N_4 matrix. Later parts of brittle fragmentation include GB and SiC fragmentation. Second-phase particles have two important effects. If they are present in front of the crack tip they weaken the microstructure because of the stress concentration caused by them. However, if they are present near GBs, they cause a crack bridging effect with an increase in strength of the microstructure.

MD analyses also reveal that the second-phase particles act as significant stress raisers, resulting in strength reduction of single-crystal and bi-crystalline Si_3N_4 blocks by a factor of almost two times. The stress concentration increases almost 1.5 times with doubling the size of SiC particles. With smaller SiC particles, the interfacial boundary in the bi-crystalline Si_3N_4 block acts as a stress reliever. However, with an increase in the size of SiC particles and with a decrease in the spacing between adjacent SiC particles, the presence of an interfacial boundary results in significant internal stress rise. This indicates that the placement of SiC particles along interfacial boundaries will not always lead to strengthening of a SiC–Si_3N_4 nanocomposite. Overall, MD analyses confirm the CFEM findings concerning the effect of second-phase SiC particles on SiC–Si_3N_4 nanocomposite strength. In addition, the analyses also indicate that the strengthening of a nanocomposite by placing second-phase particles along grain boundaries is only possible for a selective few second-phase particle sizes with interparticle spacing being another important factor.

5.8   References

1. Niihara, K., New design concept for structural ceramics – Ceramic nanocomposites. *J. Ceram. Soc. Jpn: Centennial memorial issue*, 1991, 99(10): 974–982.
2. Weimer, A.W. and Bordia, R.K., Processing and properties of nanophase SiC/Si3N4 composites. *Composites Part B*, 1999, 30: 647–655.
3. Gano, S.E., Agarwal, H., Renaud, J.E., and Tovar, A., Reliability based design using variable fidelity optimization. *Struct. Infrastruct. Engg*, 2006, 2(3–4): 247–260.
4. Gano, S.E., Renaud, J.E., and Sanders, B., Variable fidelity optimization using a kriging based scaling function. *10th AIAA/ISSMO Multidisciplinary Analysis and Optimization Conference*, Albany, New York, 2004.
5. Mejia-Rodriguez, G., Renaud, J.E., and Tomar V., A variable fidelity model

management framework for designing multiphase materials. *ASME J. Mech. Des.*, 2007, 130: 091702-1–13.

6. Mejia-Rodriguez, G., Renaud, J.E., and Tomar V., A methodology for multiscale computational design of continuous fiber SiC–Si$_3$N$_4$ ceramic composites based on the variable fidelity model management framework. *3rd AIAA Multidisciplinary Design Optimization Specialist Conference*, Honolulu, Hawaii, 2007.

7. Besson, J.L., Mayne, M., Bahloul-Hourlier, D., and Goursat, P., Nanocomposites Si$_3$N$_4$–SiCN: Influence of SiC nanocomposites on the creep behavior. *Key Engg. Mater.*, 1997, 132–136: 1970–1973.

8. Buljan, S.T., Baldoni, J.C., and Huckabee, M.L., Si$_3$N$_4$–SiC composites. *Am. Ceram. Soc. Bull.*, 1987, 66(2): 347–352.

9. Chedda, M.S., Flinn, B.D., Leckie, R., and Bordia, R.K., Effect of sub-micron sized reinforcements on the high temperature behavior of Si$_3$N$_4$ composites. *Ceram. Trans.*, 2000, 103: 223–236.

10. Lange, F.F., Effect of microstructure on strength of Si$_3$N$_4$–SiC composite system. *J. Am. Ceram. Soc.*, 1973, 56(9): 445–450.

11. Niihara, K., Izaki, K., and Kawakami, T., Hot-Pressed Si$_3$N$_4$–32%SiC nanocomposites from amorphous Si–C–N powder with improved strength above 1200°C. *J. Mater. Sci. Lett.*, 1990, 10: 112–114.

12. Rendtel, A., Hubner, H., Herrman, M., and Schubert, C., Silicon nitride/silicon carbide nanocomposite materials: II, hot strength, creep, and oxidation resistance. *J. Am. Ceram. Soc.*, 1998, 81(5): 1109–1120.

13. Sternitzke, M., Review: Structural ceramic nanocomposites. *J. Eur. Ceram. Soc.*, 1997, 17: 1061–1082.

14. Wan, J., Duan, R.-G., Gasch, M.J., and Mukherjee, A.K., Highly creep-resistant silicon nitride/silicon carbide nano-nano composites. *J. Am. Ceram. Soc.*, 2006, 89(1): 274–280.

15. Bill, J. and Aldinger, F., Precursor-derived covalent ceramics. *Adv. Mater.*, 1995, 7: 775–787.

16. Kroke, E., Li, Y.-L., Konetschny, C., Lecomte, E., Fasel, C., and Riedel, R., Silazane derived ceramics and related materials. *Mat. Sci. Engg.: R: Reports*, 2000, 26(4–6): 197–199.

17. Riedel, R., Seher, M., and Becker, G., Sintering of amorphous polymer-derived Si, N and C containing composite powders. *J. Eur. Ceram. Soc.*, 1989, 5: 113–122.

18. Riedel, R., Streker, K., and Petzow, G., In-situ polysilane-derived silicon carbide particulates dispersed in silicon nitride composite. *J. Am. Ceram. Soc.*, 1989, 72(11): 2071–2077.

19. Wan, J., Gasch, M.J., and Mukherjee, A.K., Silicon carbonitride ceramics produced by pyrolysis of polymer ceramic precursors. *J. Mater. Res.*, 2000, 15: 1657–1660.

20. Choi, H.-J., Cho, K.-S., and Lee, J.-G., R-curve behavior of silicon-nitride-titanium nitride composites. *J. Am. Ceram. Soc.*, 1997, 10(10): 2681–2684.

21. Tomar, V., Analyses of the role of the second phase SiC particles in microstructure dependent fracture resistance variation of SiC–Si$_3$N$_4$ nanocomposites. *Model. Sim. Mater. Sci. Eng.*, 2008, 16: 035001.

22. Tomar, V., Analyses of the role of grain boundaries in mesoscale dynamic

fracture resistance of SiC–Si$_3$N$_4$ intergranular nanocomposites. *Eng. Fract. Mech.*, 2008, 75: 4501–4512.

23. Bill, J., Kamphowe, T.W., Mueller, A., Wichmann, T., Zern, A., Jalowieki, A., Mayer, J., Weinmann, M., Schuhmacher, J., Mueller, K., Peng, J., Seifert, H.J., and Aldinger, F., Precursor-derived Si–(B–)C–N ceramics: thermolysis, amorphus state, and crystallization. *Appl. Organometal. Chem.*, 2001, 2001 (15): 777–793.

24. Jalowiecki, A., Bill, J., Aldinger, F., and Mayer, J., Interface characterization of nanosized B-doped Si$_3$N$_4$/SiC ceramics. *Composites Part A*, 1996, 27A: 721.

25. Farkas, D., Willemann, M., and Hyde, B., Atomistic mechanisms of fatigue in nanocrystalline metals. *Phys. Rev. Lett.*, 2005, 94: 165502.

26. Yamakov, V., Wolf, D., Phillpot, S.R., and Gleiter, H., Deformation twinning in nanocrystalline Al by moleculardynamics simulation. *Acta Mater.*, 2002, 50: 5005–5020.

27. Liao, X.Z., Zhou, F., Lavernia, E.J., He, D.W., and Zhua, Y.T., Deformation twins in nanocrystalline Al. *Appl. Phys. Lett.*, 2003, 83(24): 5062–5064.

28. Abraham, F.F., How fast can cracks move? A research adventure in materials failure using millions of atoms and big computers. *Adv. Phys.*, 2003, 52(8): 727–790.

29. Kadau, K., Germann, T.C., Lomdahl, P.S., and Holian, B.L., Microscopic view of structural phase transitions induced by shock waves. *Science*, 2002, 296: 1681.

30. Dionald, W.A.R.D., Curtin, W.A., and Yue, Q., Mechanical behavior of aluminium–silicon nanocomposites: A molecular dynamics study. *Acta Mater.*, 2006, 54(17): 4441–4451.

31. Song, M. and Chen, L., Molecular dynamics simulation of the fracture in polymer-exfoliated layered silicate nanocomposites. *Macromol. Theory Sim.*, 2006, 15(3): 238–245.

32. Tomar, V. and Zhou, M., Analyses of tensile deformation of nanocrystalline α-Fe2O3 + fcc-Al composites using classical molecular dynamics. *J. Mech. Phys. Solids*, 2007, 55: 1053–1085.

33. Zeng, Q.H., Yu, A.B., and Lu, G.Q., Molecular dynamics simulations of organoclays and polymer nanocomposites. *Int. J. Nanotechnol.*, 2008, 5(2–3): 277–290.

34. Zeng, Q.H., Yu, A.B., Lu, G.Q., and Standish, R.K., Molecular dynamics simulation of organic-inorganic nanocomposites: Layering behavior and interlayer structure of organoclays. *Chem. Mater.*, 2003, 15: 4732–4738.

35. Tsuruta, K., Totsuji, H., and Totsuji, C., Neck formation processes of nanocrystalline silicon carbide: A tight-binding molecular dynamics study. *Phil. Mag. Lett.*, 2001, 81(5): 357.

36. Tsuruta, K., Totsuji, H., and Totsuji, C., Parallel tight-binding molecular dynamics for high-temperature neck formation processes of nanocrystalline silicon carbide. *Mater. Trans.*, 2001, 42(11): 2261.

37. Mirgorodsky, A.P., Baraton, M.I., and Quintard, P., Lattice dynamics and prediction of pressure-induced incommensurate instability of a β-Si$_3$N$_4$ lattice with a simple mechanical model. *Phys. Rev. B*, 1993, 48(18): 13326–13332.

38. Lidorikis, E., Bachlechner, M.E., Kalia, R.K., Nakano, A., Vashishta, P., and Voyiadjis, G.Z., Coupling length scales for multiscale atomistic-continuum

simulations: Atomistically induced stress distributions in Si/Si_3N_4 nanopixels. *Phys. Rev. Lett.*, 2001, 87(8): 086104.

39. Tomar, V. and Zhou, M., Tension-compression strength asymmetry of nanocrystalline α-Fe_2O_3 + fcc-Al ceramic–metal composites. *Appl. Phys. Lett.*, 2006, 88: 233107 (1–3).

40. Tomar, V., Zhai, J., and Zhou, M., Bounds for element size in a variable stiffness cohesive finite element model. *Int. J. Num. Meth. Engg*, 2004, 61: 1894–1920.

41. Klopp, R.W. and Shockey, D.A., The strength behavior of granulated silicon carbide at high strain rates and confining pressure. *J. Appl. Phys.*, 1991, 70(12): 7318–7326.

42. Holmquist, T.J. and Johnson, G.R., Response of silicon carbide to high velocity impact. *J. Appl. Phys.*, 2002, 91(9): 5858–5866.

43. Walker, J., Analytically modeling hypervelocity penetration of thick ceramic targets. *Int. J. Impact Engg.*, 2003, 29(1–10): 747–755.

44. Loubens, A., Rivero, C., Boivin, P., Charlet, B., Fortunier, R., and Thomas, O., Investigation of local stress fields: Finite element modeling and high-resolution X-ray diffraction. *MRS Proc.*, 2005, 875: 0.83, doi: 10, 1577/PROC-875-08.3.

45. Minnaar, K., *Experimental and numerical analysis of damage in laminate composites under low velocity impact loading*. 2002. PhD Thesis, Georgia Institute of Technology, Atlanta, GA.

46. Tomar, V. and Zhou, M., Deterministic and stochastic analyses of dynamic fracture in two-phase ceramic microstructures with random material properties. *Eng. Fract. Mech.*, 2005, 72: 1920–1941.

47. Zhai, J., Tomar, V., and Zhou, M., Micromechanical modeling of dynamic fracture using the cohesive finite element method. *J. Engg Mater. Tech.*, 2004, 126: 179–191.

48. Xu, X.P. and Needleman, A., Numerical simulations of fast crack growth in brittle solids. *J. Mech. Phys. Solids*, 1994, 42: 1397–1434.

49. Sorensen, B.F. and Jacobsen, T.K., Determination of cohesive laws by the *J* integral approach. *Engg Frac. Mech.*, 2003, 70: 1841–1858.

50. Cornec, A., Scheider, I., and Schwalbe, K.-H., On the practical application of the cohesive zone model. *Engg Frac. Mech.*, 2003, 70: 1963–1987.

51. Espinosa, H.D., Dwivedi, S., and Lu, H.-C., Modeling impact induced delamination of woven fiber reinforced composites with contact/cohesive laws. *Comp. Meth. Appl. Mech. Engg*, 2000, 183: 259–290.

52. Niihara, K., Suganuma, K., Nakahira, A., and Izaki, K., Interfaces in Si_3N_4–SiC nanocomposites. *J. Mater. Sci. Lett.*, 1990, 9: 598–599.

53. Ajayan, P.M., Schadler, L.S., and Braun, P.V., *Nanocomposite Science and Technology*, 2003: Wiley-VCH.

54. Schwetz, K.A., Kempf, T., Saldsleder, D., and Telle, R., Toughness and hardness of LPS-SiC and LPS-SiC based composites. *Ceram. Engg Sci. Proc.*, 2004, 25(3): 579–588.

55. Messier, D.R. and Croft, W.J., *Silicon Nitride*, 1982: Army Research Laboratory, AMMRC TR 82-42.

56. Liu, X.-J., Huang, Z.-Y., Pu, X.-P., Subn, X.-W., and Huang, L.-P., Influence of planetary high-energy ball milling on microstructure and mechanical

properties of silicon nitride ceramics. *J. Am. Ceram. Soc.*, 2005, 88(5): 1323–1326.

57. Blugan, G., Hadad, Y.M., Janczak-Rusch, J., Kuebler, J., and Graulez, T., Fractography, mechanical properties, and microstructure of commercial silicon nitride–titanium nitride composites. *J. Am. Ceram. Soc.*, 2005, 88(4): 926–933.
58. Latapie, A. and Farkas, D., Molecular dynamics investigation of the fracture behavior of nanocrystalline α-Fe. *Phys. Rev. B*, 2004, 69: 134110–8.
59. Wendel, J.A. and Goddard, W.A., The Hessian biased force field for silicon nitride ceramics: Predictions of thermodynamic and mechanical properties for α- and β-Si_3N_4. *J. Chem. Phys.*, 1992, 97(7): 5048–5062.
60. Mota, F.d.B., Justo, J.F., and Fazzio, A., Hydrogen role on the properties of amorphous silicon nitride. *J. Appl. Phys.*, 1999, 86(4): 1843–1847.
61. Ching, W.-Y., Xu, Y.-N., Gale, J.D., and Ruehle, M., Ab-initio total energy calculation of α- and β-silicon nitride and the derivation of effective pair potentials with application to lattice dynamics. *J. Am. Ceram. Soc.*, 1998, 81(12): 3189–3196.
62. Fang, C.M., Wijs, G.A.d., Hintzen, H.T., and With, G.d., Phonon spectrum and thermal properties of cubic Si_3N_4 from first-principles calculations. *J. Appl. Phys.*, 2003, 93(9): 5175–5180.
63. Morkoc, H., Strite, S., Gao, G.B., Lin, M.E., Sverdlov, B., and Burns, M., Large-band-gap SIC, Ill-V nitride, and II-VI ZnSe-based semiconductor device technologies. *J. Appl. Phys.*, 1994, 76(3): 1363–1398.
64. Tersoff, J., Empirical interatomic potential for silicon with improved elastic properties. *Phys. Rev. B*, 1988, 38: 9902–9905.
65. Tersoff, J., Modeling solid-state chemistry: Interatomic potentials for multicomponent systems. *Phys. Rev. B (Rapid Comm.)*, 1989, 39(8): 5566–5568.
66. Tersoff, J., Carbon defects and defect reactions in silicon. *Phys. Rev. Lett.*, 1990, 64: 1757–1760.
67. Huang, H., Ghoniem, N.M., Wong, J.K., and Baskes, M.I., Molecular dynamics determination of defect energetics in β-SiC using three representative empirical potentials. *Model. Sim. Mater. Sci. Engg*, 1995, 1995(3): 615–627.
68. Noreyan, A., Amar, J.G., and Marinescu, I., Molecular dynamics simulations of nanoindentation of β-SiC with diamond indentor. *Mater. Sci. Engg B*, 2005, 117: 235–240.
69. Ma, Y. and Garofalini, S.H., Application of the Wolf damped Coulomb method to simulations of SiC. *J. Chem. Phys.*, 2005, 122: 094508(1–5).
70. Marian, C.M., Gastreich, M., and Gale, J.D., Empirical two-body potential for solid silicon nitride, boron nitride, and borosilazane modifications. *Phys. Rev. B*, 2000, 62(5): 3117–3124.
71. Vincent, J. and Merz, K.M., A highly portable parallel implementation of AMBER using the Message Massing Interface standard. *J. Comp. Chem.*, 1995, 11: 1420–1427.
72. Jian, W., Kaiming, Z., and Xide, X., Pair potentials for C–C, Si–Si and Si–C from inversion of the cohesive energy. *J. Phys.: Cond. Matter*, 1994, 6: 989–996.
73. Tomar, V., Atomistic modeling of the Al + Fe_2O_3 material system using classical molecular dynamics. In *Mechanical Engineering*, 2005: Georgia Institute of Technology, Alanta. P. 295.

74. Smith, W., Yong, C.W., and Rodger, P.M., DL_POLY: Application to molecular simulation. *Mol. Sim.*, 2002, 28(5): 385–471.

75. Ding, H.-Q., Karasawa, N., and Goddard III, W.A., Atomic level simulations on a million particles: The cell multipole method for Coulomb and London nonbond interactions. *J. Chem. Phys.*, 1992, 97(6): 4309–4315.

76. Wolf, D., Reconstruction of NaCl surfaces from a dipolar solution to the Madelung problem. *Phys. Rev. Lett.*, 1992, 68(22): 3315–3318.

77. Darden, T.A., York, D.M., and Pedersen, L.G., Particle mesh Ewald. An N.log (N) method for Ewald sums in large systems. *J. Chem. Phys.*, 1993, 98: 10089–10092.

78. Tomar, V. and Zhou, M., Classical molecular-dynamics potential for the mechanical strength of nanocrystalline composite fcc-Al + α-Fe_2O_3. *Phys. Rev. B*, 2006, 73: 174116 (1–16).

79. Schiøtz, J., Di Tolla, F.D., and Jacobsen, K.W., Softening of nanocrystalline metals at very small grain sizes. *Nature*, 1998, 391: 561–563.

80. Van Swygenhoven, H. and Caro, A., Plastic behavior of nanophase Ni: A molecular dynamics computer simulation. *Appl. Phys. Lett.*, 1997, 71(12): 1652–1654.

81. Spearot, D.E., Jacob, K.I., and McDowell, D.L., Nucleation of dislocations from [001] bicrystal interfaces in aluminum. *Acta Mater.*, 2005, 53: 3579–3589.

82. Schiøtz, J., Vegge, T., Di Tolla, F.D., and Jacobsen, K.W., Atomic-scale simulations of the mechanical deformation of nanocrystalline metals. *Phys. Rev. B*, 1999, 60: 11971–11983.

83. Melchionna, S., Ciccotti, G., and Holian, B.L., Hoover NPT dynamics for systems varying in shape and size. *Mol. Phys.*, 1993, 78(3): 533–544.

84. Zhou, M., A new look at the atomic level virial stress. On continuum-molecular system equivalence. *Proc. Royal Soc. London A*, 2003, 459: 2347–2392.

85. Ohji, T., Jeong, Y.-K., Choa, Y.-H., and Niihara, K., Strengthening and toughnening mechanisms of ceramic nanocomposites. *J. Am. Ceram. Soc.*, 1998, 81(6): 1453–1460.

86. Perez-Regueiro, J., Pastor, J.Y., Llorca, J., Elices, M., Miranzo, P., and Moya, J.S., Revisiting the mechanical behavior of aluminum/silicon carbide nanocomposites. *Acta Mater.*, 1998, 46(15): 5399–5411.